

# Comparison of Creep Mechanisms Between Co-Al-W- and CoNi-Based Single Crystal Superalloys at Low Temperature and High Stresses



SONG LU, ZHUOER LUO, LONGFEI LI, and QIANG FENG

TO further understand the creep performance of  $\gamma'$ -strengthened Co-based superalloys at low temperatures, the creep behaviors and mechanisms of a Co-Al-W-based and a CoNi-based single crystal superalloys (alloys 5Co and 7CoNi) were investigated at 1033 K/800 MPa and 1033 K/550 MPa based on their yield stresses, respectively. The creep behavior of alloy 5Co is characterized by forming a slow acceleration creep stage instead of a second deceleration creep stage in alloy 7CoNi after the rapid increase of creep rate in the acceleration creep stages of both alloys. The rapid shearing of multiple  $\gamma'$  precipitates by the leading partial dislocations of individual stacking faults (SFs) in alloy 5Co are responsible for the rapid increase of creep rate, while the formations of anti-phase boundary (APB)-coupled dislocation pairs and SF-APB-SF structures in  $\gamma'$  precipitates dominate the acceleration creep stage in alloy 7CoNi. The appearance of the slow acceleration creep stage in alloy 5Co can be ascribed to the generation of dislocations in the  $\gamma$  matrix and  $\gamma/\gamma'$  interface. In contrast, the interactions of individual SFs, APBs and SF-APB-SF structures in alloy 7CoNi decrease the creep rate in the second deceleration creep stage. In both alloys, the W segregation at the SF improves the creep resistance by preventing the subsequent formation of APB in the same  $\{111\}$  plane, and contributes to the dissociation of the superdislocation(s) of APB into SF-APB-SF structures in the  $\gamma'$  precipitates of alloy 7CoNi. This work will be beneficial for understanding the creep mechanism in different temperatures and further compositional optimization of  $\gamma'$ -strengthened Co-based superalloys.

<https://doi.org/10.1007/s11661-022-06892-y>

© The Minerals, Metals & Materials Society and ASM International 2022

## I. INTRODUCTION

SINCE the discovery of the ordered  $\gamma'$  phase in the Co-Al-W systems,<sup>[1]</sup>  $\gamma'$ -strengthened Co-based superalloys have been considered as candidate materials for high temperature applications due to the similar  $\gamma/\gamma'$  microstructure to Ni-based superalloys. The shearing of the  $\gamma'$  precipitate by the matrix dislocation- $a/2 < 110 >$  will introduce an anti-phase boundary (APB), thus improving the creep resistance. In addition, higher temperature capability is expected for  $\gamma'$ -strengthened Co-based superalloys due to the higher melting temperature relative to Ni-based superalloys.<sup>[2]</sup> Recent progresses have been made to further improve the  $\gamma'$

solvus temperature and environmental resistance through compositional optimization.<sup>[3–8]</sup> Typically, Ni and Cr elements are added into the Co-Al-W-based systems, forming the CoNi-based superalloys.<sup>[3,4]</sup> Considering the actual service environment of Ni-based superalloys, good creep performances in a temperature range (973 ~ 1373 K) are demanded for  $\gamma'$ -strengthened Co-based superalloys.<sup>[9]</sup> Most researches have been performed to improve the creep resistance of  $\gamma'$ -strengthened Co-based single crystal superalloys at high temperatures (> 1173 K).<sup>[10–16]</sup> Specially, a dependence of the Co/Ni ratio on the creep properties and deformation mechanisms of  $\gamma'$  precipitates was detected at 1173 K.<sup>[16–18]</sup> However, up to now, minimal works have been reported on the low temperature creep properties of the Co-Al-W- or CoNi-based<sup>[19]</sup> single crystal superalloys.

Combined with the researches in Ni-based single crystal superalloys, the creep process at low temperatures is sensitive to the levels of applied stress and composition.<sup>[20,21]</sup> When the threshold stress is exceeded, the creep rate will increase rapidly, resulting in a high strain in the early creep stage. Moreover, Co and Re elements were reported to promote the

SONG LU, ZHUOER LUO, LONGFEI LI, and QIANG FENG are with the Beijing Advanced Innovation Center for Materials Genome Engineering, State Key Laboratory for Advanced Metals and Materials, University of Science and Technology Beijing, Beijing 100083, P.R. China. Contact e-mail: qfeng@skl.ustb.edu.cn

Manuscript submitted August 13, 2022; accepted October 30, 2022.

Article published online November 23, 2022

aforementioned creep process by lowering the formation energy of stacking faults (SFs) in the  $\langle 112 \rangle \{111\}$  slip systems of  $\gamma'$  precipitates.<sup>[20,22]</sup> Normally, complex or superlattice intrinsic and extrinsic stacking faults (CISF, CESF, SISF and SESF)<sup>[23–25]</sup> are the typical deformation substructures in Ni-based single superalloys at low temperature and high stress.<sup>[26]</sup> Specially, a dislocation ribbon consisting of SISF-APB-SESF has been observed in the  $\gamma/\gamma'$  microstructure.<sup>[26–28]</sup> This configuration was assumed to pass through the  $\gamma'$  precipitate without leaving any dislocation debris and control the initiated high strain.<sup>[20,27]</sup> For  $\gamma'$ -strengthened Co-based single crystal superalloys, the high Co content gives rise to a low SF energy as indicated by the high density of SF during the creep process at high temperatures ( $> 1123$  K).<sup>[10,12,15,29]</sup> Additionally, the addition of Ni element into the  $\gamma'$ -strengthened Co-based single crystal superalloys promotes the formation of APB at 1123 K with reduced W content.<sup>[14,30]</sup> However, how these factors affect the creep performance of  $\gamma'$ -strengthened Co-based single crystal superalloys at low temperature and high stress is still unclear.

After the rapid increase of creep rate in the early stage, some strengthening mechanisms will take over the following creep process.<sup>[27,31,32]</sup> Generally, the expansions of SFs in multiple slip systems are activated in this stage, and the creep rate decreases until it reaches a minimum. The interactions of SFs in different  $\{111\}$  planes were proposed to improve the deformation resistance of  $\gamma'$  precipitates in Ni-based<sup>[33]</sup> and  $\gamma'$ -strengthened Co-based single crystal superalloys.<sup>[10,12]</sup> Some qualitative and quantitative studies have been conducted to evaluate the strengthening effect of the SF interactions in  $\gamma'$ -strengthened Co-based single crystal superalloys at 1123 ~ 1273 K.<sup>[13,34,35]</sup> While in Ni-based single crystal superalloys, related researches have indicated that the dislocations at the  $\gamma/\gamma'$  interfaces<sup>[20]</sup> and in the  $\gamma'$  precipitates<sup>[32]</sup> also affect the decrease of the creep rate at 1023 K. Recently, elemental segregation at the SF has been proposed to increase or decrease the creep resistance by triggering the local phase transformation.<sup>[36–39]</sup> W/Ta segregation-assisted  $\gamma' \rightarrow \chi/\eta$  phase transformations at SFs inhibit the formation of APBs or twins, thus improving the creep resistance.<sup>[36,38]</sup> On the contrary, Co/Cr segregation-assisted  $\gamma' \rightarrow \gamma$  phase transformation has a negative effect.<sup>[36]</sup> Therefore, understanding the dominant deformation substructures and effects of local elemental segregation on creep resistance at low temperature and high stress will be significant for developing  $\gamma'$ -strengthened Co-based single crystal superalloys.

In this work, two types of  $\gamma'$ -strengthened Co-based single crystal superalloys, Co-Al-W- and CoNi-based, were crept at 1033 K and high stresses. Then, the creep behaviors of two alloys were analyzed based on the  $\gamma/\gamma'$  microstructure, deformation substructure and elemental segregation behavior in different creep stages. Finally, the creep mechanisms of investigated Co-Al-W- and CoNi-based single crystal superalloys were revealed and compared. This work will be important for

understanding the creep mechanism at low temperature and compositional optimization of  $\gamma'$ -strengthened Co-based superalloys.

## II. EXPERIMENTAL

The nominal compositions of the experimental Co-Al-W- and CoNi-based alloys are Co-7Al-8W-1Ta-4Ti (at pct), referred to as alloy 5Co, and Co-30Ni-11Al-4W-4Ti-1Ta-5Cr (at pct) (abbreviated as alloy 7CoNi), respectively. All the experimental single crystal superalloys were melted and subsequently directionally solidified along [001] direction with the conventional Bridgman method. Subsequently, alloy 7CoNi was heat treated in the following process: 1523 K/24 hours, air cooling (AC) 1273 K/4 hours, AC + 1073 K/16 hours, AC. A typical  $\gamma/\gamma'$  microstructure was obtained with a  $\gamma'$  volume fraction ( $V_{\gamma'}$ ) of  $87.9 \pm 4.2$  pct, which was calculated from the area fraction ( $A_{\gamma'}$ ) based on the morphology of  $\gamma'$  precipitate ( $V_{\gamma'} = (A_{\gamma'})^{3/2}$ ).<sup>[12]</sup> The area (S) equivalent widths of the  $\gamma'$  precipitate ( $D_{\gamma'} = (S_{\gamma'})^{1/2}$ ) and  $\gamma$  channel ( $D_{\gamma}$ ) are  $478 \pm 76$  nm and  $9 \pm 6$  nm, respectively. The detail about the heat treatment process of alloy 5Co has been previously reported and its  $V_{\gamma'}$ ,  $D_{\gamma'}$ , and  $D_{\gamma}$  are  $79.1 \pm 3.5$  pct,  $175 \pm 43$  nm, and  $14 \pm 4$  nm, respectively.<sup>[12,34,40]</sup>

To exclude the orientation dependence on the creep behavior at low temperature/high stress, specimens with [001] orientation (5 deg ~ 8 deg deviation near the [001]–[111] boundary) were selected to tensile-creep deformed at 1033 K with their ~ 90 pct yield stresses, 800 MPa and 550 MPa for alloys 5Co and 7CoNi, respectively. Then, some interrupted tests were performed based on the variation of creep rate to investigate the creep mechanisms of both alloys. All the samples used for the characterizations were extracted parallel to the tensile axis ([100] and [110] directions) from the gage section of the creep specimens. The  $\gamma/\gamma'$  microstructure was analyzed using a ZEISS SUPRA 55 field-emission scanning electron microscope (SEM). Transmission electron microscope (TEM) thin foils were mechanically ground to ~ 60  $\mu$ m and finally thinned by a twin-jet polisher in a solution of 7 pct HClO<sub>4</sub> + 4 pct CH<sub>3</sub>COOH + 89 pct C<sub>2</sub>H<sub>5</sub>OH (by volume) at – 25 °C and 30 V with a current of 30 ~ 80 mA. Then, the deformation substructures were observed in a Tecnai G2 F30 S-TWIN transmission electron microscope (TEM) operating at 300 kV. In addition, high angle annular dark field (HAADF) imaging and energy dispersive X-ray spectroscopy (EDX) mapping of the  $\gamma/\gamma'$  microstructure and deformation substructures were also conducted using an FEI Talos F200X scanning transmission electron microscopy (STEM) equipped with a Super-X energy dispersive X-ray spectroscopy four-quadrant detector. All the elements were quantified by the integrated line scans through Cliff-Lorimer analysis<sup>[41]</sup> using K $\alpha$  energies for Co, Ni, Al Ti and Cr, L $\alpha$  energy (8.398 keV) for W, and M $\alpha$  energy (1.713 keV) for Ta.

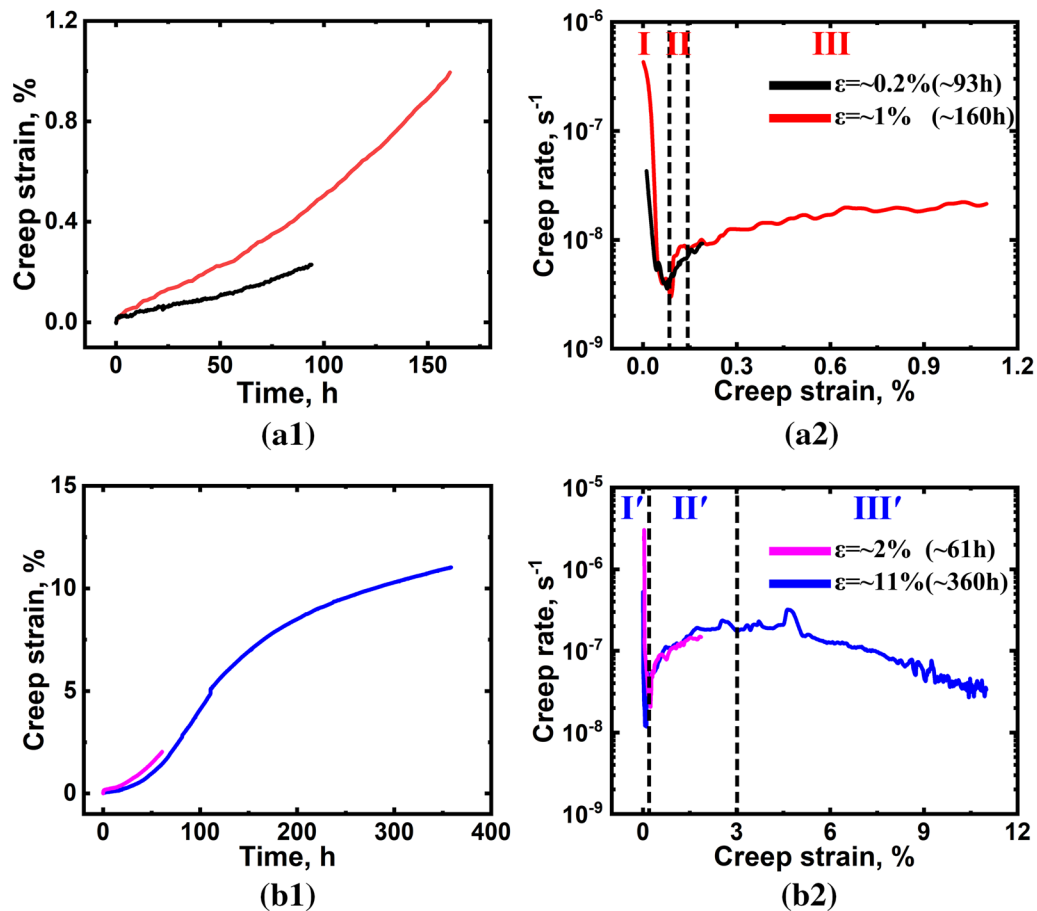


Fig. 1—Creep curves of alloys 5Co and 7CoNi at 1033 K, respectively. (a) Alloy 5Co at 1033 K/800 MPa; (b) alloy 7CoNi at 1033 K/550 MPa; (1) creep strain vs. time; (2) creep rate vs. creep strain. The vertical dashed black lines note the boundaries between the different creep stages (Color figure online).

### III. RESULTS

#### A. Creep Properties

Figure 1 shows the creep curves of alloys 5Co and 7CoNi at 1033 K, respectively. For alloy 5Co, the creep test was performed at  $\varepsilon = \sim 1$  pct and  $t = \sim 160$  hours at 1033 K/800 MPa [Figure 1(a1)]. Then, the variation of creep rate with the creep strain is plotted in Figure 1(a2) based on the creep strain vs. time curves. The creep rate decreased rapidly in the deceleration creep stage (I) until it reached a minimum value ( $\sim 2.8 \times 10^{-9} \text{ s}^{-1}$ ). After that, the creep rate increased rapidly, labeled as the acceleration creep stage (II). Interestingly, the increased speed of creep rate slowed down as the creep proceeded. Thus, a slow acceleration creep stage (III) was defined, and lasted until creep fracture ( $\varepsilon = \sim 11$  pct with  $t = \sim 854$  hours, see details in Supplementary Materials- Figure S1).

In contrast, the creep strain vs. time and creep rate vs. creep strain curves of alloy 7CoNi at 1033 K/550 MPa are plotted in Figures 1(b1) and (b2), respectively. Compared to Figure 1(a1), a higher interrupted creep strain was selected to give an overview of the creep process in alloy 7CoNi. The deceleration creep stage (I')

ended with a local minimum creep rate of  $\sim 1 \times 10^{-8} \text{ s}^{-1}$ , followed by an acceleration creep stage (II'). The creep rate rapidly increased to  $\sim 2 \times 10^{-7} \text{ s}^{-1}$ , and decreased slowly in the second deceleration creep stage (III'). Based on the variation of creep rate with the creep strain, the boundaries between the different creep stages in two alloys were labeled by the vertical dashed black lines in Figures 1(a2) and (b2), respectively.

Additional interrupted creep tests were performed in two acceleration stages (II/II') ( $\varepsilon = \sim 0.2$  pct and  $t = \sim 93$  hours for alloy 5Co, while  $\varepsilon = \sim 2$  pct and  $t = \sim 61$  hours for alloy 7CoNi), as shown in the black line of Figure 1(a) and pink line of Figure 1(b), respectively. Deviation of creep strain vs. creep strain curve between  $\varepsilon = \sim 0.2$  pct and  $\varepsilon = \sim 1$  pct in alloy 5Co is likely attributed to the slightly different crystal orientations. The creep curves of two experimental alloys are reproducible, as indicated by more interrupted creep tests (Figure S1).

#### B. Deformation Structures in Acceleration Creep Stages

Figures 2(a) and (b) exhibit the SEM images of the longitudinal  $\gamma/\gamma'$  microstructures in the acceleration creep stages of alloys 5Co and 7CoNi, respectively. No

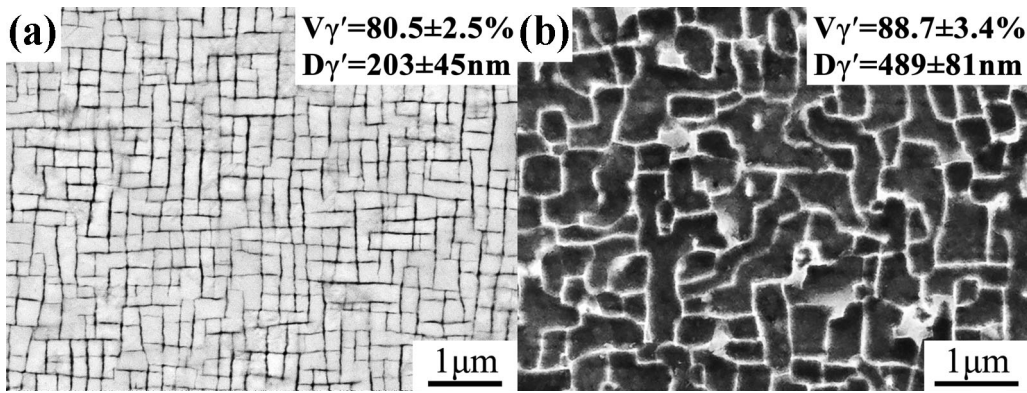


Fig. 2—SEM images showing the longitudinal  $\gamma/\gamma'$  microstructures in the acceleration creep stages of alloys 5Co and 7CoNi, respectively. (a) Alloy 5Co at 1033 K/800 MPa with  $\varepsilon = \sim 0.2$  pct and  $t = \sim 93$  hours; (b) alloy 7CoNi at 1033 K/550 MPa with  $\varepsilon = \sim 2$  pct and  $t = \sim 61$  hours.

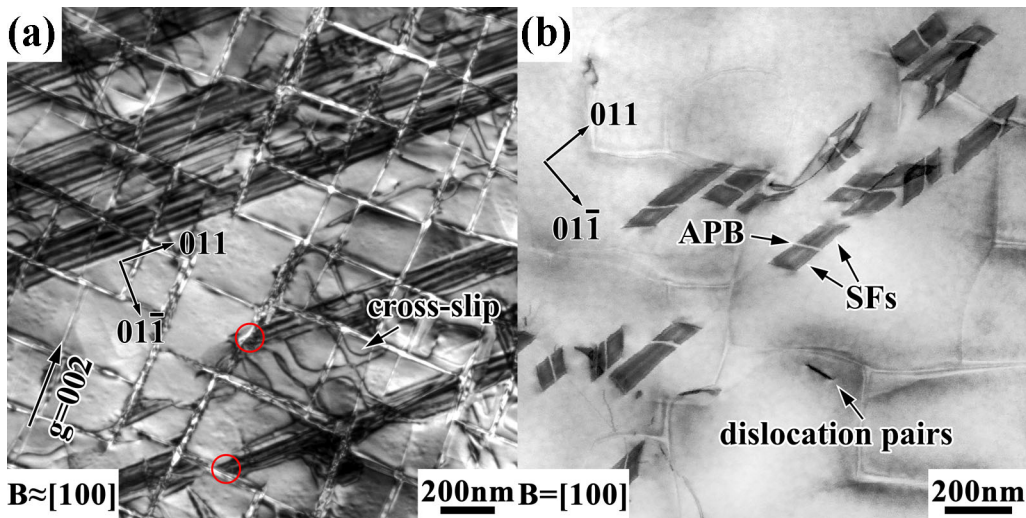


Fig. 3—TEM images showing the deformation substructures in the acceleration creep stages of alloys 5Co and 7CoNi, respectively. (a) Alloy 5Co at 1033 K/800 MPa with  $\varepsilon = \sim 0.2$  pct and  $t = \sim 93$  hours, TEM,  $B \approx [100]$ ,  $g = 002$ ; (b) alloy 7CoNi at 1033 K/550 MPa with  $\varepsilon = \sim 2$  pct and  $t = \sim 61$  hours, STEM,  $B = [100]$ .

noticeable change of  $\gamma/\gamma'$  microstructure was observed compared to the heat treatment state. For alloy 5Co at 1033 K/800 MPa with  $\varepsilon = \sim 0.2$  pct and  $t = \sim 93$  hours, the  $\gamma'$  precipitate presents with a bright contrast after the  $\gamma$  matrix was etched and remains cuboidal with a  $D_{\gamma'}$  of  $203 \pm 45$  nm. The  $V_{\gamma'}$  and  $D_{\gamma}$  are  $80.5 \pm 2.5$  pct and  $18 \pm 10$  nm, respectively, as shown in Figure 2(a). The  $\gamma/\gamma'$  microstructure of alloy 7CoNi [Figure 2(b)] was characterized by the connection of etched cuboidal  $\gamma'$  precipitates with a dark contrast after crept at 1033 K/550 MPa with  $\varepsilon = \sim 2$  pct and  $t = \sim 61$  hours. The  $V_{\gamma'}$ ,  $D_{\gamma'}$  and  $D_{\gamma}$  are  $88.7 \pm 3.4$  pct,  $489 \pm 81$  nm, and  $8 \pm 5$  nm, respectively.

Figure 3 shows the TEM images of the deformation substructures corresponding to the  $\gamma/\gamma'$  microstructures in Figure 2. The deformation substructure of alloy 5Co was dominated by the  $\gamma/\gamma'$  interfacial dislocations and SFs expanding through the  $\gamma/\gamma'$  microstructure, as shown in Figure 3(a) with  $B \approx [100]$  and  $g = 002$ . The matrix dislocation cross slipped in different  $\{111\}$  planes

as evidenced by the  $\langle 011 \rangle$ -oriented interfacial dislocations with a corner of 90 deg [arrow in Figure 3(a)].<sup>[10,12,29]</sup> The SF mainly expanded along  $[011]$  direction as viewed from  $B \approx [100]$ , which indicates activations of slip systems on the  $(\bar{1}\bar{1}1)$  or  $(11\bar{1})$  planes. A similar case was also observed under  $B \approx [001]$ . This indicates only one primary slip system was active based on the crystal geometry in the TEM image. Interactions of SFs were occasionally detected in this stage. Further analysis shows that the SFs mainly formed through the shearing of  $\gamma'$  precipitates by the leading partial dislocations at the  $\gamma/\gamma'$  interfaces, as red circled in Figure 3(a). Moreover, most leading partial dislocations continuously passed through multiple  $\gamma'$  precipitates and  $\gamma$  matrix. Then, continuous SFs formed in the  $\gamma/\gamma'$  microstructure. For alloy 7CoNi, rare  $\gamma/\gamma'$  interfacial dislocations were observed, and the deformation substructures in  $\gamma'$  precipitates controlled the whole acceleration creep stage, as shown in Figure 3(b). Two SFs were connected by an APB in the  $\gamma'$  precipitate and

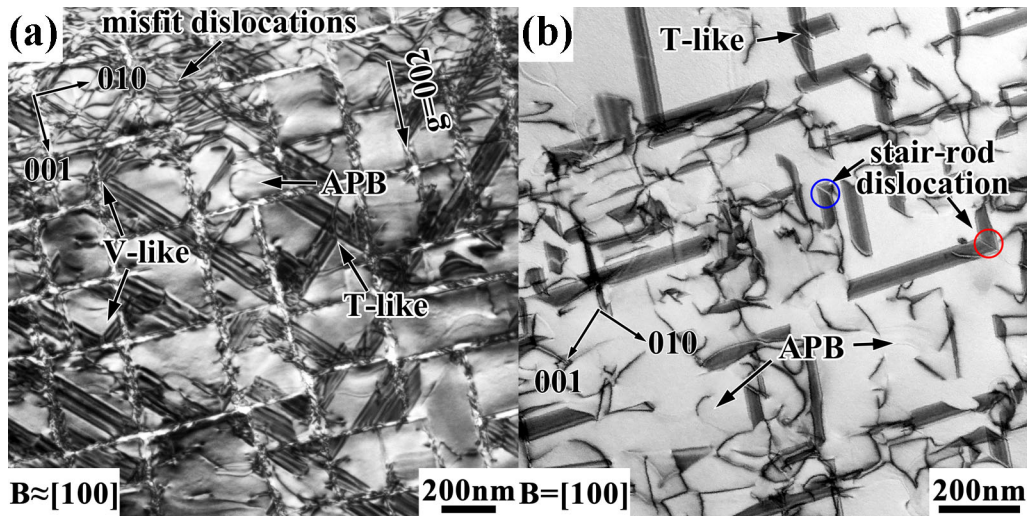


Fig. 4—TEM images showing the deformation substructures after the acceleration creep stages. (a) Alloy 5Co at 1033 K/800 MPa with  $\epsilon = \sim 1$  pct and  $t = \sim 160$  hours, TEM,  $B \approx [100]$ ,  $g = 002$ ; (b) alloy 7CoNi at 1033 K/550 MPa with  $\epsilon = \sim 11$  pct and  $t = \sim 360$  hours, STEM,  $B = [100]$ .

formed a ribbon-like configuration (SF-APB-SF). Of note is that most of the SF-APB-SF structures were confined inside one  $\gamma'$  precipitate without connecting with the  $\gamma/\gamma'$  interface. Similar to alloy 5Co, the ribbon-like configuration mainly expanded along the [011] direction as seen from  $B = [100]$  in the STEM mode, and rare interactions were observed. Besides the SF-APB-SF configurations, APB-coupled dislocation pairs were also observed in  $\gamma'$  precipitates, as labeled in Figure 3(b). It should be mentioned that the SF-APB-SF and dislocation pairs were non-uniformly distributed in the  $\gamma'$  precipitates. The multiple TEM images indicate a comparable density for the two configurations above (images not shown in this study).

### C. Deformation Structures After the Acceleration Stages

After the acceleration stages, no noticeable evolution of  $\gamma/\gamma'$  microstructure was found in the slow acceleration stage of alloy 5Co and second deceleration stage of alloy 7CoNi, respectively. The images are not shown here. Figures 4(a) and (b) exhibit the corresponding deformation substructures of alloys 5Co and 7CoNi, respectively. For alloy 5Co, the interaction of  $\gamma/\gamma'$  interfacial dislocations became more active in Figure 4(a) than the case in Figure 3(a). Some mismatch-orientation,  $\langle 100 \rangle$ , dislocations were found, but no perfect interfacial dislocation network formed as viewed from  $B \approx [100]$  and  $g = 002$ . The SFs across multiple  $\gamma'$  precipitates can still be observed, while most of them were confined in one  $\gamma'$  precipitate. Moreover, the SFs in the multiple slip systems were active and interacted with each other as labeled by V- and T-like in Figure 4(a). Specially, the two SFs in the V-like configurations seemed to interact at the  $\gamma/\gamma'$  interfaces, not inside the  $\gamma'$  precipitates as widely reported in Refs.<sup>[10,34,42]</sup> This will be further discussed in the following sections. In addition, some individual superdislocations also sheared into the  $\gamma'$  precipitates, leaving APBs behind. The

density of individual APB is lower than that of the SF. Figure 4(b) shows typical deformation substructures of alloy 7CoNi in the second deceleration creep stage. At  $\epsilon = \sim 11$  pct and  $t = \sim 360$  hours, rare interfacial dislocations were observed. While in the  $\gamma'$  precipitates, different from alloy 5Co, the density of individual APB is comparable to or higher than that of the SF-APB-SF structure. Moreover, the individual SFs were also observed with a lower density than the SF-APB-SF structures. All three types of deformation substructures interacted in the  $\gamma'$  precipitates. Some leading partial dislocations of SF-APB-SF structures and individual SFs cross slipped and formed stair-rod dislocations (V-like configurations) inside  $\gamma'$  precipitates as labeled by the red and blue circles, respectively. In addition, T-like configurations can also be observed. The leading partial dislocations of SFs and superdislocations of APBs were not observed to penetrate through the planar defects in both alloys for now.

### D. Segregation Behaviors

To further study the effect of alloy composition on the creep performance, the elemental segregation behaviors in alloys 5Co and 7CoNi were investigated. Only the results of alloy 7CoNi were shown in this work to simplify the analysis and avoid repetition with other published works. The elemental segregation behaviors in alloy 5Co have been reported in other works at 1273 K,<sup>[34,40]</sup> and no noticeable difference was detected at 1033 K (see details in Supplementary Materials-Figure S2).

Figure 5 shows the HAADF-STEM image and EDX elemental mapping (at pct) of the  $\gamma/\gamma'$  microstructure in alloy 7CoNi after heat treatment at  $B = [100]$ . Co and Cr elements were segregated to the  $\gamma$  matrix, while Ni, Al, W, Ta and Ti elements were enriched in the  $\gamma'$  precipitate. This segregation behavior is similar to other CoNi-based superalloys.<sup>[13,35,42]</sup> The elemental

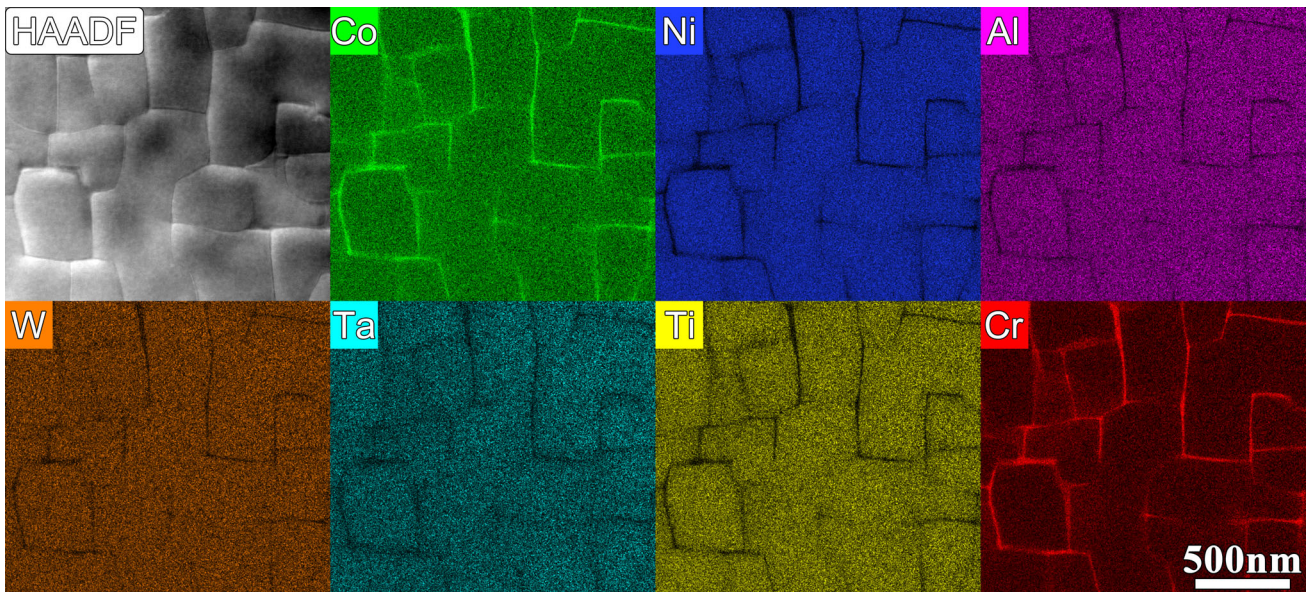


Fig. 5—HAADF-STEM image and EDX elemental mapping (at pct) of the  $\gamma/\gamma'$  microstructure in alloy 7CoNi after heat treatment at  $B = [100]$  (Color figure online).

partitioning behaviors between alloys 5Co and 7CoNi were similar for the Co, W, Ta and Ti elements. The Al element was evenly distributed in the  $\gamma/\gamma'$  microstructure of alloy 5Co.

As mentioned in Figure 3(b), the SF-APB-SF structure was one of the dominant deformation substructures in the acceleration creep stage of alloy 7CoNi at 1033 K/550 MPa. Therefore, this configuration and its elemental segregation behavior were further analyzed in the edge-on view of SFs, (110). Figure 6(a) exhibits the HAADF-STEM image and EDX elemental mapping (at pct) of the SF-APB-SF structure in a  $\gamma'$  precipitate of alloy 7CoNi at 1033 K/550 MPa with  $\varepsilon = \sim 2$  pct and  $t = \sim 61$  hours,  $B = [110]$ . The two SFs (SF-1 and SF-2) were identified with the intrinsic nature (see details in Supplementary Materials-Figure S3) and located at the two parallel (111) planes, respectively. In contrast, the APB connected them and located in a curved plane. The SFs present a lighter contrast. In contrast, the APB seems invisible due to the similar contrast with the surrounding  $\gamma'$  region. Figures 6(b) and (c) show the integrated line scan profiles perpendicular to the SF-1 and APB in the HAADF-STEM image of Figure 6(a). The results show that the SF-1 was rich in Co, W and Cr elements, with a depletion of Ni and Al elements. In contrast, Ta and Ti elements had almost a uniform distribution between the SF-1 and the  $\gamma'$  precipitate [Figure 6(a) and (b)]. Similar segregation behavior was also observed for the SF-2 (not shown here). For the APB, the  $\gamma$  formers (Co and Cr) were enriched, while the  $\gamma'$  formers (Ni, Al, W, Ta, and Ti) were depleted, as shown in Figures 6(b) and (c). It should be mentioned that the expansion distance of APB was variable, and sometimes the distance between the two SFs was too small to tell whether they located at the same slip plane. The elemental segregation behavior at the SF of alloy 5Co (Figure S2) was similar to Figure 6(b) for the Al,

W, Ta and Ti elements, while Co was slightly depleted at the SF due to the high content ( $\sim 78$  at pct) in the  $\gamma'$  precipitate.<sup>[34,40]</sup>

#### IV. DISCUSSIONS

As shown in Figure 1, the creep behaviors of investigated Co-Al-W- and CoNi-based single crystal superalloy at low temperature and high stress are different. The creep behavior of alloy 5Co is similar to that at high temperature and low stress,<sup>[10,12]</sup> while the case in alloy 7CoNi is comparable to that in Ni-based superalloys.<sup>[43]</sup> Generally, this is associated with the interaction between the  $\gamma/\gamma'$  microstructure and deformation substructure. Moreover, many researchers have demonstrated that the local elemental segregation behavior strongly influences the formation and evolution of deformation substructure during the creep process.<sup>[36,40,44,45]</sup> Therefore, to further clarify the creep mechanisms of Co-Al-W- and CoNi-based single crystal superalloy at low temperature and high stresses, the featured creep stages will be discussed in the following sections based on the aforementioned factors.

##### A. Deformation Mechanisms in the Acceleration Creep Stages

The creep process in Ni-based superalloys at low temperature and high stress usually generates a high creep strain in the early creep stage. This has been proposed to be associated with the formation of dislocation ribbon (SISF-APB-SESF) with the sum of the Burgers vector of a  $\langle 112 \rangle$ ,<sup>[26,28,46]</sup> which is a full dislocation for the ordered  $\gamma'$  precipitate. The ordered lattice will be restored by the trailing partial dislocation of SESF. In addition, a critical stress triggers the high

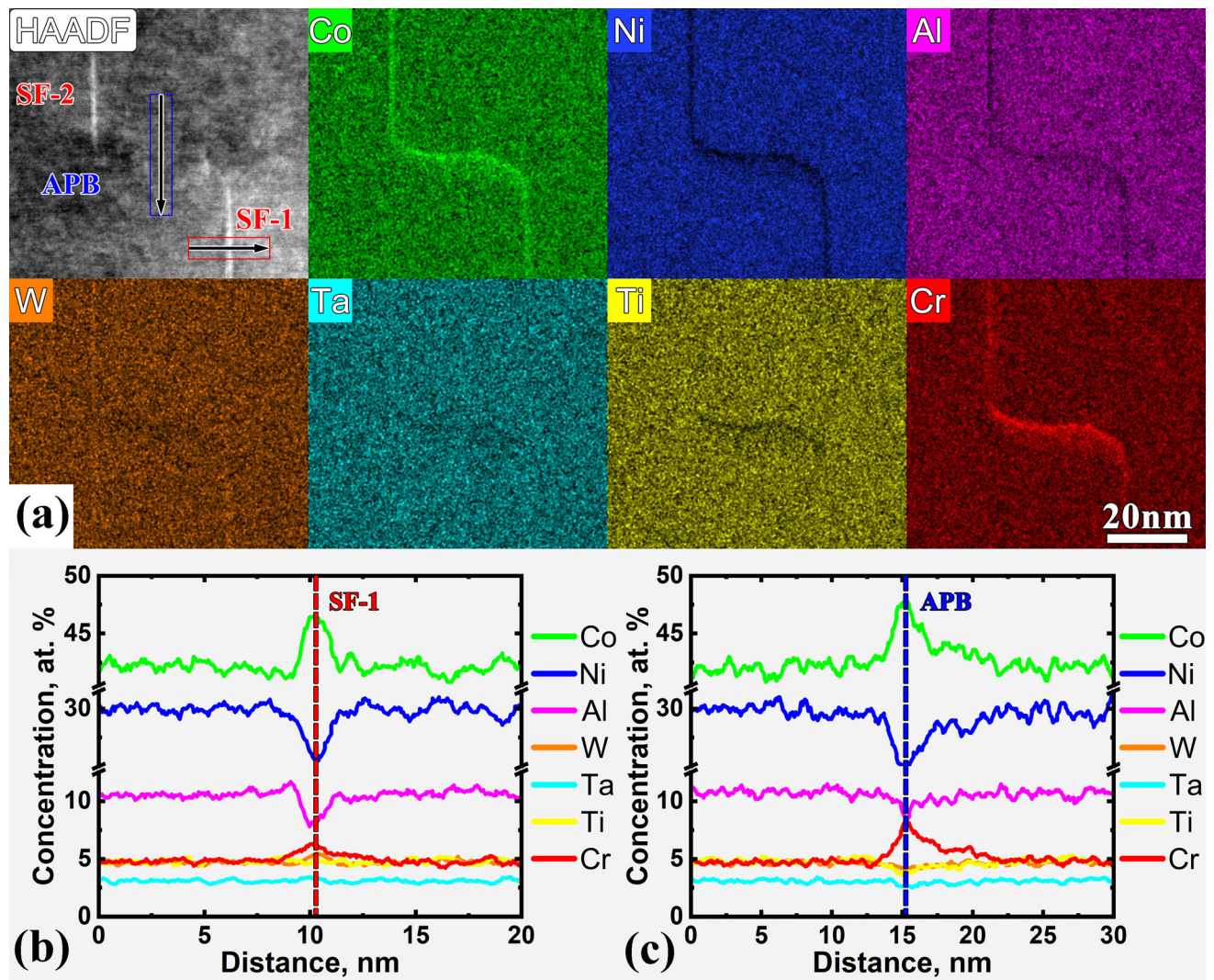


Fig. 6—HAADF-STEM image and EDX analysis of the SF-APB-SF structure in a  $\gamma'$  precipitate of alloy 7CoNi at 1033 K/550 MPa with  $\varepsilon = \sim 2.0$  pct and  $t = \sim 61$  hours,  $B = [110]$ . (a) HAADF-STEM image and EDX maps (at pct); integrated line scan profiles perpendicular to the (b) SF-1 and (c) APB in (a) (Color figure online).

creep rate, normally  $> 550$  MPa in some commercial Ni-based superalloys.<sup>[9,20]</sup> The initiated high creep strain is susceptible in the Re-containing single crystal superalloy due to the contribution of Re element to the decrease of SF energy.<sup>[20,43]</sup>

In the current research, the creep tests were performed based on the yield stresses, and acceleration creep stages occurred in both experimental alloys. However, the deformation substructures dominating the rapid increase of creep rate differed between the investigated Co-Al-W- and CoNi-based single crystal superalloys (Figure 3). In alloy 5Co, multiple  $\gamma'$  precipitates were continuously sheared by the leading partial dislocations of individual SFs, accompanied by the cross-slip of matrix dislocations. This deformation mechanism is similar to the case at 1173 K/420 MPa.<sup>[10,29]</sup> While in alloy 7CoNi, rare matrix dislocations were detected. This difference can be attributed to the narrower  $D_\gamma$  (see Sections II and III-A), resulting in a higher Orowan stress required for the dislocation glide in the matrix<sup>[47]</sup>

of alloy 7CoNi than that in alloy 5Co. On the other hand, the yield stress results indicate a low critical stress for the shearing of  $\gamma'$  precipitates in alloy 7CoNi, although high  $V_\gamma$  was obtained. These factors rapidly transform creep deformation into the  $\gamma'$  precipitates from the  $\gamma$  matrix. Thus, it is the formation and evolution of deformation substructures (dislocation pairs and SF-APB-SF structures) in the  $\gamma'$  precipitates that dominate the creep process in the acceleration creep stage of alloy 7CoNi. Moreover, the SF and APB can expand in the different planes, as shown in Figure 6, and the whole SF-APB-SF structure is mainly confined within one  $\gamma'$  precipitate instead of connecting with the  $\gamma/\gamma'$  interface [Figure 3(b)]. Combined with the comparable density of dislocation pairs and SF-APB-SF structures in  $\gamma'$  precipitates, a possible evolution process is proposed, as shown in Figure 7.

First, two close-packed dislocations of the  $a/2 < 110 >$  type deposit at the  $\gamma/\gamma'$  interface; then, one  $a/2 < 110 >$  dislocation shears into the  $\gamma'$  precipitate,

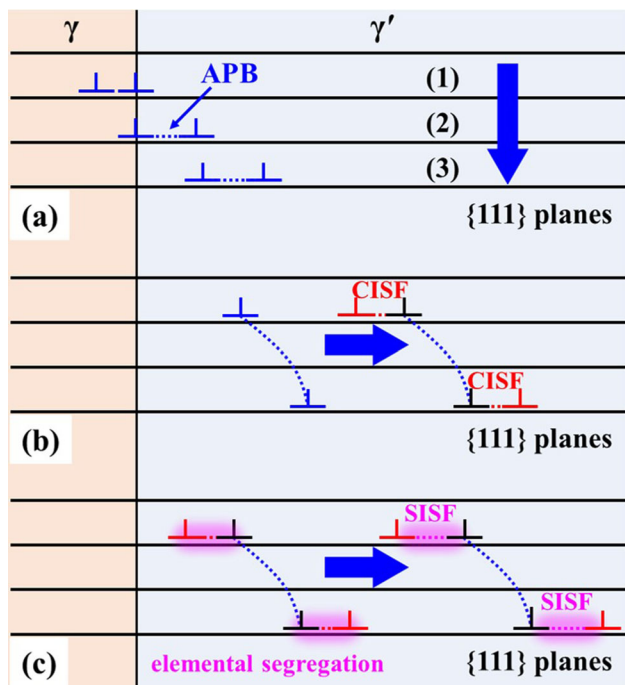


Fig. 7—A schematic of dislocation pairs and SF-APB-SF structure formation processes in the  $\gamma'$  precipitate of alloy 7CoNi at 1033 K/550 MPa. (a) Shearing of the  $\gamma'$  precipitate by the dislocation pairs; (b) formation of expansion of APB towards the  $\{100\}$  planes from  $\{111\}$  planes and dissociations of superdislocations; (c) segregation-assisted expansions of leading partial dislocations (Color figure online).

leaving an APB behind; finally, the second  $a/2 < 110 >$  dislocation also shears the  $\gamma'$  precipitate in the same  $\{111\}$  plane to restore the  $\gamma'$  lattice, as labeled by (1), (2), and (3) in Figure 7(a), respectively. The aforementioned process generates APB-coupled dislocation pairs moving in  $\{111\}$  planes. However, the APB prefers to expand toward the  $\{100\}$  planes from the original  $\{111\}$  planes by the cross-slip process of superdislocation due to the lower APB energy in the  $\{100\}$  planes than that in the  $\{111\}$  planes.<sup>[48,49]</sup> Theoretically, the superdislocation can also cross-slip back to the  $\{111\}$  from  $\{100\}$  planes if the difference of APB energies between the two planes is favorable. Thus, the morphology of APB typically presents with a curved line.<sup>[30,40]</sup> While, in most  $\gamma'$ -L1<sub>2</sub> phase strengthened superalloys, the superdislocation was assumed to further dissociate into the CISF-coupled leading and trailing Shockley partial dislocations in  $\{111\}$  planes based on the dislocation energy reduction criterion ( $(a/2 < 01\bar{1} >)^2 > (a/6 < 12\bar{1} >)^2 + a/6 < \bar{1}1\bar{2} >^2$ ). The trailing partial dislocation connects the APB in the curved plane and CISF in one  $\{111\}$  plane, and is pinned by the two planar defects [Figure 7(b)], terminating APB expansion. Thus, a sessile configuration (Kear-Wilsdorf (KW) lock) forms and has been proposed to contribute to the anomalous yield behavior in the superalloys.<sup>[50,51]</sup> Normally, the dissociation width of superdislocation is extremely narrow due to energy unfavorable for the expansion of the CISF. Recently, segregation-assisted reordering process (CISF  $\rightarrow$  SISF)

or phase transformation ( $\gamma' \rightarrow \chi$ ) have been proposed to lower the intrinsic SF energy and facilitate the propagation of the leading dislocation(s) through the  $\gamma'$  precipitates.<sup>[36,38,40,52]</sup> Thus, combined with the results shown in Figure 6(a), the non-coplanar SF-APB-SF structure forms, and leading partial dislocations of the two CISF/SISFs (Figure S3) in the sessile KW lock further expand in the  $\gamma'$  precipitates [Figure 3(b)] with the assistance of the elemental segregation at SFs [Figure 7(c)].

It should be mentioned that this formation mechanism is different from the widely reported dislocation ribbon (SISF-APB-SESF), wherein the dislocation configurations can be considered as  $a/2 < 112 >$  type dislocation pairs, not the  $a/2 < 110 >$  type shown in Figure 7(a). Moreover, the three planar defects locate at the same or the parallel consecutive  $\{111\}$  planes, and the APB forms after the shearing of  $\gamma'$  precipitates by the trailing partial dislocation of SISF, which is different from the formation process of KW lock [Figure 7(b)]. In addition, a non-coplanar SSF-APB structure has also been reported in alloy 5Co at 1255 K/248 MPa.<sup>[40]</sup> Although they have similar non-coplanar configurations, the SSF-APB in alloy 5Co can further evolve into a ...SISF-APB... repetitive structure. Moreover, no APB-coupled dislocation pairs configurations were detected in alloy 5Co at 1255 K/248 MPa. Most importantly, the nucleation of APB superdislocation is closely related to the segregation-assisted local  $\gamma$  phase transformation near the leading partial dislocation of SF<sup>[40]</sup> instead of matrix dislocation shearing  $\gamma'$  precipitates in alloy 7CoNi.

Considering the above discussions, it can be concluded that once the  $\gamma'$  precipitate is sheared by the deformation substructures, whether individual leading partial dislocations of SFs or other complex dislocation ribbons, such as SF-APB-SF or dislocation pairs configurations, the creep process will transform into an acceleration stage. It should be mentioned that high strain was not detected in the early creep stage of alloy 5Co, although an acceleration stage occurs. In fact, the creep strain in the acceleration stage of alloy 5Co is lower than 0.2 pct [Figure 1(a2)]. Related analysis is underway and will be further explained in the future.

## B. Strengthening Mechanism at Low Temperature and High Stress

Generally, after the acceleration stage, the creep rate will slowly decrease until it reaches a minimum in Ni-based superalloys at low temperature and high stress.<sup>[20,21,33,53,54]</sup> However, there seems no consensus about the dominant strengthening mechanism in this stage. Some researchers indicate that the interactions of SFs in multiple slip systems are responsible for this strengthening process.<sup>[33,54]</sup> However, Rae *et al.* have also found that the creep rate decreased long before the activation of conjugate slip systems of the SFs.<sup>[21]</sup> Moreover, the formation of dislocations able to shear into the  $\gamma'$  precipitate is thought to be the rate-limiting process based on the calculation of activation energy.<sup>[20]</sup>

In this study, although the Co-Al-W-based alloy didn't show a decrease of creep rate, the increased speed of creep rate still decreased after the acceleration stage, which means activations of some strengthening mechanisms and results in a slow acceleration creep stage [Figure 1(a2)]. Theoretically, the creep rate can be determined as  $\dot{\epsilon} = \rho b v$ , where  $b$  is the equivalent Burgers vector, while  $\rho$  and  $v$  are the equivalent density and speed of the mobile dislocation in the  $\gamma/\gamma'$  microstructure, respectively. Compared to the acceleration stage,  $b$  is assumed to increase by the higher density of a  $2 < 110 >$  matrix dislocation relative to the partial dislocation.  $\rho$  increases as indicated by the higher density of dislocations in the  $\gamma$  matrix or  $\gamma/\gamma'$  interface, and partial dislocations in  $\gamma'$  precipitates [Figure 4(a)].  $v$  is dependent on the dislocations in the  $\gamma/\gamma'$  microstructure. The formation of dislocation networks and pile-up of dislocations will lower the mobility of the matrix dislocation. In the  $\gamma'$  precipitate, the interactions of SFs prevent the slip of leading partial dislocations of individual SFs, such as T-like configurations. Moreover, the  $\gamma/\gamma'$  interface can also constrain the expansion of individual SFs, and most of the leading partial dislocations were captured by the  $\gamma/\gamma'$  interfaces. In addition, the V-like configuration was also observed, but the stair-rod dislocation seemed to locate at the  $\gamma/\gamma'$  interface, not inside the  $\gamma'$  precipitate. Typically, the stair-rod dislocation in the V-like configuration originates from the cross-slip process of partial dislocation. This is similar to the case in some Cu alloys, where the partial dislocation can bounce back or towards another plane when countering a barrier.<sup>[55]</sup> Thus, the  $\gamma/\gamma'$  interface can act as a barrier triggering the cross-slip process. When the slip speed of partial dislocation is high enough, after it counters the  $\gamma/\gamma'$  interface, the partial dislocation will dissociate into a stair-rod dislocation at the  $\gamma/\gamma'$  interface, and another partial dislocation expands in the conjugated  $\{111\}$  plane. The  $v$  of leading partial dislocations in the slow acceleration stage is assumed to be lower than that in the acceleration stage due to the re-distribution of inter stress onto the all four octahedral planes. Otherwise, all the leading partial dislocations will penetrate through the  $\gamma/\gamma'$  interfaces and continuously shear the subsequent  $\gamma/\gamma'$  microstructures. Moreover, the aforementioned generation of interfacial dislocations will also prevent the penetration of  $\gamma/\gamma'$  interfaces by the leading partial dislocations.<sup>[20]</sup> Considering the variation of creep rate in the slow acceleration stage and above analysis, although the interactions of SFs improve the deformation resistance of the  $\gamma'$  precipitate, their strengthening effect cannot completely compensate for the weakening effect induced by the high-speed generation of dislocations. The  $\rho$  in the  $\gamma$  matrix or  $\gamma/\gamma'$  interface dominates the slow acceleration stage in alloy 5Co.

In contrast, the variation of creep rate in the experimental CoNi-based single crystal superalloy is similar to that of the typical Ni-based superalloys.<sup>[26,43]</sup> The creep rate decreased after the acceleration creep stage, as shown in Figure 1(b2). As mentioned in Section IV-A, different from alloy 5Co, due to the higher  $V_{\gamma'}$  and narrower  $D_{\gamma'}$ , the deformation of  $\gamma'$

precipitate controls the primary creep process in alloy 7CoNi. T-like configurations consisting of individual SFs or SF-APB-SF structures improve the creep resistance by preventing the expansion of partial dislocations in their original slip systems. This strengthening mechanism is similar to alloy 5Co. While for the V-like configuration, the partial dislocations of both individual SFs or SF-APB-SF structures in alloy 7CoNi cross slipped and left a stair-rod dislocation inside the  $\gamma'$  precipitate instead of at the  $\gamma/\gamma'$  interface as alloy 5Co. This can be ascribed to the larger  $D_{\gamma'}$  in alloy 7CoNi ( $\sim 489$  nm) than that in alloy 5Co ( $\sim 203$  nm), which provides a higher possibility for the cross-slip processes of the partial dislocations. Besides the individual SFs and SF-APB-SF structures, many individual APBs formed in the  $\gamma'$  precipitate. Compared to the APB-coupled dislocation pairs, the individual APB introduces a larger area of planar defect and can more easily interact with the individual SFs and SF-APB-SF ribbons. The complex interactions between the three types of planar defects decrease their expansion rate in the  $\gamma'$  precipitate, thus improving the creep resistance. In addition, it should be noted that, for both alloys, the formation and evolution of deformation substructures strongly depend on the elemental segregation behaviors at the SF and APB, and will be further discussed in the following section.

### C. Effect of Elemental Segregation Behavior on the Deformation Substructure

Local elemental segregation behavior has been reported to affect the creep resistance by changing the formation energy of deformation substructures.<sup>[34,36,40,44,52,56,57]</sup> Especially at low temperature and high stress, the W or Ta segregations at the SFs were reported to prevent the formation of dislocation ribbons or twins.<sup>[36,44]</sup> In addition, the elemental segregation at the planar or linear defects may trigger the local phase transformation, which improves or decrease creep resistance.<sup>[36,40,52,57]</sup> Moreover, some novel deformation mechanisms may be activated, as reported in a Co-Al-W-based superalloys.<sup>[40]</sup>

As discussed in Sections IV-B and IV-C, the primary deformation substructures in alloys 5Co and 7CoNi differ. This can be explained by the segregation behaviors in the  $\gamma'$  precipitates and at the planar defects. At 1033 K/800 MPa, the high Co content ( $\sim 78$  at pct) in the  $\gamma'$  precipitates of alloy 5Co<sup>[40]</sup> leads to a low SF energy. Thus, the  $\gamma'$  precipitates prefer to be sheared by the leading partial dislocations of SFs. Moreover, the local W segregation at the SFs can trigger the local  $\gamma' \rightarrow \chi/\eta$  phase transformations, further stabilizing the SF configuration in the  $\gamma'$  precipitate.<sup>[36,38]</sup> Meanwhile, the high W content ( $\sim 10$  at pct, Figure S2) at the SF increases the APB energy and prevents the further shearing of the trailing partial dislocations of SFs into the  $\gamma'$  precipitates, which generates an APB following the SF in the same  $\{111\}$  plane. Therefore, only rare individual APBs were observed in the  $\gamma'$  precipitates during the slow acceleration creep stage.

In contrast, the CoNi-based superalloys normally have lower formation energy of APB than SF due to the Ni addition and low W content. The APB was considered as the main deformation substructure during creep at 1173 K.<sup>[15,30]</sup> This is similar to the case in alloy 7CoNi at 1033 K/550 MPa. The individual APBs were prevalent in the second deceleration creep stage [Figure 4(b)] and even subsequent creep processes (not shown in this study). In addition, combined with the elemental segregation behavior shown in Figure 6, the W element is enriched at the SF and depleted at the APB, similar to the alloy 5Co. Thus, it is difficult to form an APB following a W-segregated SF. Moreover, this further evidenced the formation mechanism of the SF-APB-SF structure shown in Figure 7, where the SF forms later than the APB-coupled dislocation pairs in the acceleration creep stage.

## V. CONCLUSIONS

The creep behaviors were investigated in a Co-Al-W-based and a CoNi-based single crystal superalloys, respectively, at 1033 K with high stresses. The creep mechanisms were revealed and compared based on the  $\gamma/\gamma'$  microstructure, dislocation substructure and elemental segregation behavior. The following conclusions can be drawn:

- Based on the variation of creep rate, the creep processes of alloys 5Co and 7CoNi were similar from the initial deceleration to the subsequent acceleration creep stages. After that, the creep behavior of alloy 5Co is characterized by a slow increase of creep rate, while the alloy 7CoNi goes through a second deceleration creep stage.
- The rapid shearing of  $\gamma'$  precipitates by the deformation substructures decreases the creep resistance and contributes to the corresponding acceleration creep stages in the two types of superalloys. The expansion of individual SFs in the  $\gamma/\gamma'$  microstructure dominates the acceleration creep stage in alloy 5Co at 1033 K/800 MPa. In contrast, dislocation pairs and non-coplanar SF-APB-SF structure formations in  $\gamma'$  precipitates are responsible for the acceleration creep stage in alloy 7CoNi at 1033 K/550 MPa.
- After the acceleration creep stage, the weakening effect of high-speed generation of dislocations in the  $\gamma$  matrix and  $\gamma/\gamma'$  interface cannot be entirely compensated by the strengthening effect of SF interactions in  $\gamma'$  precipitates, which results in a slow acceleration creep stage in alloy 5Co. The high  $V_\gamma$  and large  $D_\gamma$  in alloy 7CoNi promote the interaction of individual SFs, APBs and non-coplanar SF-APB-SF structures in  $\gamma'$  precipitates, thus controlling the decrease of creep rate in the second deceleration creep stage.
- The W segregation at the SF restrains the subsequent formation of W-depleted APB in the same {111} plane for both alloys 5Co and 7CoNi, improving the creep resistance. This also contributes

to the formation of non-coplanar SF-APB-SF structure by promoting the dissociation of the superdislocation(s) of APB and further propagation of leading partial dislocation(s) in the  $\gamma'$  precipitate of alloy 7CoNi.

## ACKNOWLEDGMENTS

The authors would like to acknowledge the support provided by the National Natural Science Foundation of China (Grant Nos.: 5217011046, 52201100, 51771019 and 92060113), China Postdoctoral Science Foundation (Grant No.: 2022M710346), Science and Technology on Advanced High Temperature Structural Materials Laboratory (Grant No.: 6142903210207), National Key Research and Development Program of China (Grant No.: 2017YFB0702902) and Key-Area Research and Development Program of Guangdong Province (Grant No.: 2019B010943001).

## DATA AVAILABILITY

The raw/processed data required to reproduce these findings cannot be shared at this time as the data also forms part of an ongoing study.

## CONFLICT OF INTEREST

The authors declare no conflicts of interest in this paper.

## SUPPLEMENTARY INFORMATION

The online version contains supplementary material available at <https://doi.org/10.1007/s11661-022-06892-y>.

## REFERENCES

1. J. Sato, T. Omori, K. Oikawa, I. Ohnuma, R. Kainuma, and K. Ishida: *Science*, 2006, vol. 312, pp. 90–1.
2. A. Suzuki, H. Inui, and T.M. Pollock: *Annu. Rev. Mater. Res.*, 2015, vol. 45, pp. 345–68.
3. W. Li, L. Li, S. Antonov, C. Wei, J.-C. Zhao, and Q. Feng: *J. Alloys Compd.*, 2021, vol. 881, p. 160618.
4. W. Li, L. Li, S. Antonov, and Q. Feng: *Mater. Des.*, 2019, vol. 180, p. 107912.
5. S. Neumeier, L.P. Freund, and M. Göken: *Scripta Mater.*, 2015, vol. 109, pp. 104–07.
6. F. Pyczak, A. Bauer, M. Göken, U. Lorenz, S. Neumeier, M. Oehring, J. Paul, N. Schell, A. Schreyer, A. Stark, and F. Symanzik: *J. Alloys Compd.*, 2015, vol. 632, pp. 110–15.
7. A. Bauer, S. Neumeier, F. Pyczak, and M. Göken: *Adv. Eng. Mater.*, 2014, vol. 17, pp. 748–54.
8. C.H. Zenk, N. Volz, A. Bezold, L.-K. Huber, Y.M. Eggeler, E. Spiecker, M. Göken, and S. Neumeier: in *Book*. S. Tin, M. Hardy,

- J. Clews, J. Cormier, Q. Feng, J. Marcin, C. O'Brien, and A. Suzuki, eds., Wiley, Hoboken, 2020, pp. 909–19.
9. R.C. Reed: *The superalloys fundamentals and applications*, Cambridge University Press, Cambridge, 2006.
  10. H. Zhou, L. Li, S. Antonov, and Q. Feng: *Mater. Sci. Eng. A*, 2020, vol. 772, 138791.
  11. F. Xue, H.J. Zhou, Q.Y. Shi, X.H. Chen, H. Chang, M.L. Wang, and Q. Feng: *Scripta Mater.*, 2015, vol. 97, pp. 37–40.
  12. S. Lu, S. Antonov, L.F. Li, and Q. Feng: *Metall. Mater. Trans. A*, 2018, vol. 49, pp. 4079–89.
  13. M. Lenz, Y.M. Eggeler, J. Müller, C.H. Zenk, N. Volz, P. Wollgramm, G. Eggeler, S. Neumeier, M. Göken, and E. Spiecker: *Acta Mater.*, 2019, vol. 166, pp. 597–610.
  14. Y.M. Eggeler, J. Müller, M.S. Titus, A. Suzuki, T.M. Pollock, and E. Spiecker: *Acta Mater.*, 2016, vol. 113, pp. 335–49.
  15. M.S. Titus, Y.M. Eggeler, A. Suzuki, and T.M. Pollock: *Acta Mater.*, 2015, vol. 82, pp. 530–39.
  16. N. Volz, C.H. Zenk, N. Karpstein, M. Lenz, E. Spiecker, M. Göken, and S. Neumeier: *Philos. Mag.*, 2022, vol. 112, pp. 718–44.
  17. C.H. Zenk, S. Neumeier, M. Kolb, N. Volz, S.G. Fries, O. Dolotko, I. Povstugar, D. Raabe, and M. Göken: in *Superalloys 2016*, M. Hardy, E. Huron, U. Glatzel, B. Griffin, B. Lewis, C. Rae, V. Seetharaman, and S. Tin, eds., TMS, 2016, pp. 971–80.
  18. C.H. Zenk, S. Neumeier, N.M. Engl, S.G. Fries, O. Dolotko, M. Weiser, S. Virtanen, and M. Göken: *Scripta Mater.*, 2016, vol. 112, pp. 83–6.
  19. M.S. Titus, L.H. Rettberg, and T.M. Pollock: in *Superalloys 2016*, M. Hardy, E. Huron, U. Glatzel, B. Griffin, B. Lewis, C. Rae, V. Seetharaman, and S. Tin, eds., TMS, 2016, pp. 141–48.
  20. G.L. Drew, R.C. Reed, K. Kakehi, and C.M.F. Rae: in *Superalloys 2004*, K.A. Green, T.M. Pollock, H. Harada, T.E. Howson, R.C. Reed, J.J. Schirra, and S. Walston, eds., TMS, 2004, pp. 127–36.
  21. C.M.F. Rae, N. Matan, M.A. Rist, D.C. Cox, and R.C. Reed: *Metall. Mater. Trans. A*, 2000, vol. 31, pp. 2219–228.
  22. H. Murakami, T. Yamagata, H. Harada, and M. Yamazaki: *Mater. Sci. Eng. A*, 1997, vol. 223, pp. 54–8.
  23. L. Kovarik, R.R. Unocic, J. Li, P. Sarosi, C. Shen, Y. Wang, and M.J. Mills: *Prog. Mater. Sci.*, 2009, vol. 54, pp. 839–73.
  24. V.A. Vorontsov, L. Kovarik, M.J. Mills, and C.M.F. Rae: *Acta Mater.*, 2012, vol. 60, pp. 4866–78.
  25. V.A. Vorontsov, R.E. Voskoboynikov, and C.M.F. Rae: *Philos. Mag.*, 2012, vol. 92, pp. 608–34.
  26. C.M.F. Rae and R.C. Reed: *Acta Mater.*, 2007, vol. 55, pp. 1067–081.
  27. D. Qi, D. Wang, K. Du, Y. Qi, L. Lou, J. Zhang, and H. Ye: *J. Alloys Compd.*, 2018, vol. 735, pp. 813–20.
  28. X. Wu, A. Dlouhy, Y.M. Eggeler, E. Spiecker, A. Kostka, C. Somsen, and G. Eggeler: *Acta Mater.*, 2018, vol. 144, pp. 642–55.
  29. H.J. Zhou, H. Chang, and Q. Feng: *Scripta Mater.*, 2017, vol. 135, pp. 84–7.
  30. Y.M. Eggeler, M.S. Titus, A. Suzuki, and T.M. Pollock: *Acta Mater.*, 2014, vol. 77, pp. 352–59.
  31. R.C. Reed, N. Matan, D.C. Cox, M.A. Rist, and C.M.F. Rae: *Acta Mater.*, 1999, vol. 47, pp. 3367–81.
  32. X. Wu, P. Wollgramm, C. Somsen, A. Dlouhy, A. Kostka, and G. Eggeler: *Acta Mater.*, 2016, vol. 112, pp. 242–60.
  33. J. Yu, J.R. Li, J.Q. Zhao, M. Han, Z.X. Shi, S.Z. Liu, and H.L. Yuan: *Mater. Sci. Eng. A*, 2013, vol. 560, pp. 47–53.
  34. S. Lu, S. Antonov, L.F. Li, C.P. Liu, X.N. Zhang, Y.F. Zheng, H.L. Fraser, and Q. Feng: *Acta Mater.*, 2020, vol. 190, pp. 16–28.
  35. M.S. Titus, A. Mottura, G. Babu Viswanathan, A. Suzuki, M.J. Mills, and T.M. Pollock: *Acta Mater.*, 2015, vol. 89, pp. 423–37.
  36. T.M. Smith, B.S. Good, T.P. Gabb, B.D. Esser, A.J. Egan, L.J. Evans, D.W. McComb, and M.J. Mills: *Acta Mater.*, 2019, vol. 172, pp. 55–65.
  37. T.M. Smith, B.D. Esser, B. Good, M.S. Hooshmand, G.B. Viswanathan, C.M.F. Rae, M. Ghazisaeidi, D.W. McComb, and M.J. Mills: *Metall. Mater. Trans. A*, 2018, vol. 49, pp. 4186–98.
  38. T.M. Smith, B.D. Esser, N. Antolin, A. Carlsson, R.E. Williams, A. Wessman, T. Hanlon, H.L. Fraser, W. Windl, D.W. McComb, and M.J. Mills: *Nat. Commun.*, 2016, vol. 7, p. 13434.
  39. J. He, C.H. Zenk, X. Zhou, S. Neumeier, D. Raabe, B. Gault, and S.K. Mäkinen: *Acta Mater.*, 2020, vol. 184, pp. 86–99.
  40. S. Lu, S. Antonov, F. Xue, L.F. Li, and Q. Feng: *Acta Mater.*, 2021, vol. 215, 117099.
  41. H. Hoefl and P. Schwaab: *X-Ray Spectrom.*, 1988, vol. 17, pp. 201–08.
  42. A. Bezold, N. Volz, M. Lenz, N. Karpstein, C.H. Zenk, E. Spiecker, M. Göken, and S. Neumeier: *Acta Mater.*, 2022, vol. 227, p. 117702.
  43. X. Wu, S.K. Mäkinen, C.H. Liebscher, G. Dehm, J. Rezaei Mianroodi, P. Shanthraj, B. Svendsen, D. Burger, G. Eggeler, D. Raabe, and B. Gault: *Nat. Commun.*, 2020, vol. 11, p. 389.
  44. T.M. Smith, B.D. Esser, N. Antolin, G.B. Viswanathan, T. Hanlon, A. Wessman, D. Mourer, W. Windl, D.W. McComb, and M.J. Mills: *Acta Mater.*, 2015, vol. 100, pp. 19–31.
  45. J. He, M. Zou, L. Li, X. Wang, and Q. Feng: *Mater. Lett.*, 2020, vol. 262, p. 127042.
  46. H. Long, Y. Liu, D. Kong, H. Wei, Y. Chen, and S. Mao: *J. Alloys Compd.*, 2017, vol. 724, pp. 287–95.
  47. T.M. Pollock and A.S. Argon: *Acta Metall. Mater.*, 1992, vol. 40, pp. 1–30.
  48. J.E. Saal and C. Wolverton: *Acta Mater.*, 2016, vol. 103, pp. 57–62.
  49. R. Kikuchi and J.W. Cahn: *Acta Metall.*, 1979, vol. 27, pp. 1337–53.
  50. T. Kruml, E. Conforto, B. Lo Piccolo, D. Caillard, and J.L. Martin: *Acta Mater.*, 2002, vol. 50, pp. 5091–101.
  51. A. Suzuki and T.M. Pollock: *Acta Mater.*, 2008, vol. 56, pp. 1288–297.
  52. D. Barba, T.M. Smith, J. Miao, M.J. Mills, and R.C. Reed: *Metall. Mater. Trans. A*, 2018, vol. 49, pp. 4173–85.
  53. F.D. León-Cázares, F. Monni, and C.M.F. Rae: *Acta Mater.*, 2020, vol. 199, pp. 209–24.
  54. S.H. Zhang, D. Wang, J. Zhang, and L.H. Lou: *J. Mater. Sci. Technol.*, 2012, vol. 28, pp. 229–33.
  55. Q.J. Li, J. Li, Z.W. Shan, and E. Ma: *Acta Mater.*, 2016, vol. 119, pp. 229–41.
  56. Y. Rao, T.M. Smith, M.J. Mills, and M. Ghazisaeidi: *Acta Mater.*, 2018, vol. 148, pp. 4173–85.
  57. L. Liliensten, P. Kürsteiner, J.R. Mianroodi, A. Cervellon, J. Moverare, M. Segersäll, S. Antonov, and P. Kontis: in *Superalloys 2020*, S. Tin, M. Hardy, J. Clews, J. Cormier, Q. Feng, J. Marcin, C. O'Brien, and A. Suzuki, eds., Wiley, Hoboken, 2020, pp. 41–51.

**Publisher's Note** Springer Nature remains neutral with regard to jurisdictional claims in published maps and institutional affiliations.

Springer Nature or its licensor (e.g. a society or other partner) holds exclusive rights to this article under a publishing agreement with the author(s) or other rightsholder(s); author self-archiving of the accepted manuscript version of this article is solely governed by the terms of such publishing agreement and applicable law.